Tech Science Press

Numerical Investigations on the Impact of Turbulent Prandtl Number and Schmidt Number on Supersonic Combustion

Yongkang Zheng[1,2,*] and Chao Yan[1]

[1]National Key Laboratory of Computational Fluid Dynamics, Beihang University, Beijing, 100191, China
[2]State Key Laboratory of Aerodynamics, Mianyang, 621000, China
*Corresponding Author: Yongkang Zheng. Email: zykbuaa@buaa.edu.cn

Abstract: The flow field inside the combustor of a scramjet is highly complicated and the related turbulent Prandtl and Schmidt numbers have a significant impact on the effective numerical prediction of such dynamics. As in many cases researchers set these parameters on the basis of purely empirical laws, assessing their impact (via parametric numerical simulations) is a subject of great importance. In the present work, in particular, two test cases with different characteristics are selected for further evaluation of the role played by these non-dimensional numbers: Burrows-Kurkov case and DLR case. The numerical results indicate that these parameters influence ignition location. Moreover, the temperature distribution is more sensitive to them than to H_2O mass fraction and velocity distributions.

1 Introduction

For accurate predictions on scramjet engines with turbulence models, calculation requires the turbulent Prandtl number (Pr_t) and the Schmidt number (Sc_t) for the purpose of accounting for turbulence/chemistry interactions [1]. Eklund demonstrates that predicting Pr_t and Sc_t for turbulence models should be as part of the solution, with the assumption that low Schmidt number can lead to unstart phenomena in combustor while high Schmidt number can result in blowout phenomena for flame [2].

However, traditional turbulence models, which are applied mostly to scramjet engine simulations, only take velocity fluctuations into consideration and these two parameters as constants. Since the variance of temperature and the mixing between fuel and oxidizer are inversely proportional to Pr_t and Sc_t, respectively, these two dominant parameters have remarkable effect on the conduction and diffusion processes.

Among the researches, both variable and constant Pr_t and Sc_t are adopted as the critical factors for scramjet flow field prediction. Baurle chooses the Pr_t and the Sc_t as 0.9 and 0.5 respectively to control the turbulent mass and energy transport within the simulation of cavity flameholder using a hybrid Reynolds-averaged/large-eddy scheme [3]. Edwards sets both two parameters as 0.7 while simulating a

three-dimensional flame/shock wave interaction problem [4]. Gao assumes these two parameters as 0.9 in supersonic turbulent combustion flows with the flamelet model [5]. As in many cases researchers set these parameters on the basis of purely empirical laws, assessing their impact is of great importance. On the other hand, Xiao proposes a strategy about variable Pr_t and Sc_t and applies it to model scramjet flows [1]. Two additional equations are introduced into the governing system to calculate Pr_t and Sc_t as a part of the solution, which avoids involving the assumed probability density function into supersonic combustion flows. Variable Pr_t is implemented in Xiao's research on heat transfer prediction for separated flows [6] and variable turbulent Schmidt Number is implemented in Large-eddy simulations by Ingenito [7]. Jiang et al. investigates some of the eddy dissipation combustion results obtained with the Pr_t and Sc_t varying from 0.25 to 0.85 and the calculated results are in good agreement with the experimental database [8]. Therefore, it can be concluded that the numerical solution is affected greatly by the selection of the Pr_t and Sc_t. For the express purpose of providing reliable evidence for further research, it is inevitable and significant to evaluate the affection of these tow parameters on the flow field prediction of scramjet configuration.

In this paper, the sensitivity analysis of turbulent Prandtl number Pr_t and Schmidt number Sc_t for supersonic combustion is performed, and ignition location, temperature and combustion efficiency are focused as well. Two representative experimental cases are selected and the numerical results with different combinations of parameters are compared in detail. Some statistical analysis on the affection of the two critical factors are also performed.

2 Numerical Methods

A finite volume in-house code developed by the authors is utilized to simulate all the numerical cases. The compressible governing equations, including the mass, momentum, energy and species transport equations, are solved using Reynolds-averaged Navier-Stokes simulations (RANS). The finite-rate chemistry model is adopted as combustion model in this study. Main algorithms of this code are presented follows:

2.1 Governing Equations

The Favre-averaged conservation equations in the Cartesian coordinate are interpreted as:

Continuity equation:

$$\frac{\partial \rho}{\partial t} + \frac{\partial \rho u_j}{\partial x_j} = 0 \tag{1}$$

Momentum equation:

$$\frac{\partial \rho u_i}{\partial t} + \frac{\partial \rho u_i u_j}{\partial x_j} = -\frac{\partial p}{\partial x_i} + \frac{\partial \tau_{ij}}{\partial x_j} \tag{2}$$

Energy equation:

$$\frac{\partial \rho E}{\partial t} + \frac{\partial \rho H u_j}{\partial x_j} = \frac{\partial}{\partial x_j}\left(\left(\lambda + \frac{\mu_t C_p}{Pr_t}\right)\frac{\partial T}{\partial x_j}\right) + \frac{\partial}{\partial x_j}\left(\sum_{s=1}^{ns}\left(\rho D_s + \frac{\mu_t}{Sc_t}\right)h_s\frac{\partial Y_s}{\partial x_j}\right) + \frac{\partial \tau_{ij}u_i}{\partial x_j} \tag{3}$$

Species continuity equation:

$$\frac{\partial \rho Y_s}{\partial t} + \frac{\partial \rho Y_s u_j}{\partial x_j} = \frac{\partial}{\partial x_j}\left(\left(\rho D_s + \frac{\mu_t}{Sc_t}\right)\frac{\partial Y_s}{\partial x_j}\right) + \dot{\omega}_s \tag{4}$$

where ρ, u_j, p, T are the density, velocity component in j^{th} Cartesian, pressure and temperature, respectively. Y_s, D_s, h_s are the mass fraction, diffusion coefficient and enthalpy per unit mass of species s, respectively. λ, E and H are the thermal conductivity coefficient, total energy per unit mass of mixture and total enthalpy per unit mass of mixture, respectively. τ_{ij} is the viscous stress tensor defined as:

$$\tau_{ij} = \mu \left(\frac{\partial u_i}{\partial x_j} + \frac{\partial u_j}{\partial x_i} \right) - \frac{2}{3} \mu \frac{\partial u_k}{\partial x_k} \delta_{ij} \tag{5}$$

where δ_{ij} is the Kronecker symbol.

The source term $\dot{\omega}_s$ is given with finite rate chemical model as follows:

$$\dot{\omega}_s = M_s \sum_{j=1}^{nr} \left(\beta_{js} - \alpha_{js} \right) \left(R_j - R_{-j} \right) \tag{6}$$

where M_s is the molecular weight of the species s, α_{js} and β_{js} are the stoichiometric coefficients of the related species in the jth reaction. R_j and R_{-j} the forward and backward net rate of the jth reaction respectively:

$$R_j = K_j \prod_{s=1}^{ns} \left(\frac{\rho_s}{M_s} \right)^{\alpha_{js}}, R_{-j} = K_{-j} \prod_{s=1}^{ns} \left(\frac{\rho_s}{M_s} \right)^{\beta_{js}} \tag{7}$$

where K_j is the forward rate coefficient of the jth reaction, and K_{-j} is the backward rate coefficient of the jth reaction. The state equation of mixture gas is provide in the form:

$$p = R_u T \sum_{s=1}^{ns} \frac{\rho Y_s}{M_s} \tag{8}$$

where R_u is the universal gas constant, M_s is the molecular weight of species s.

The static enthalpy and the specific heat at constant pressure are considered with temperature and species dependent thermodynamic properties as follow:

$$h = \sum_{s=1}^{ns} h_s Y_s, C_p = \sum_{s=1}^{ns} C_{p,s} Y_s \tag{9}$$

where h_s, $C_{p,s}$ are the enthalpy and specific heat at constant pressure of species s, modeled with a polynomial function of static temperature.

For each species, thermal conductivity and molecular viscosity are calculated with Sutherlands formula. Wilkes formula [9] is then applied to calculate the mixture thermal conductivity and the mixture molecular viscosity. Besides, mass diffusivity is calculated according to the kinetic theory as follows [10]:

$$\rho D_s = \frac{1 - Y_s}{1 - X_s} \frac{\mu}{Sc} \tag{10}$$

where X_s is the mole fraction of species s.

The total energy per unit mass of mixture E and total enthalpy per unit mass of mixture H are defined as:

$$H = h + \frac{1}{2} u_j u_j, E = H - \frac{p}{\rho} \tag{11}$$

2.2 Turbulence Model

As shown in previous investigations, turbulence model plays very important roles in prediction of the flow field variables and the interaction between turbulence and combustion for supersonic combustion simulations. According to its good performance for less computational cost and more numerical robustness [11], Menter's shear stress transport (SST) model [12] has extensive applications in engineering and thus employed in this paper. The SST turbulence model introduces the original $k - \omega$ model inside boundary layer region and switches into the standard $k - \epsilon$ model outside boundary layer region as well as in free shear flows [12]. The transport equations used for SST turbulence model take the form:

$$\frac{\partial \rho k}{\partial t} + \frac{\partial \rho u_j k}{\partial x_j} = \frac{\partial}{\partial x_j}\left[(\mu + \sigma_k \mu_t)\frac{\partial k}{\partial x_j}\right] + P_k - \beta^* \rho \omega k \tag{12}$$

$$\frac{\partial \rho \omega}{\partial t} + \frac{\partial \rho u_j \omega}{\partial x_j} = \frac{\partial}{\partial x_j}\left[(\mu + \sigma_\omega \mu_t)\frac{\partial \omega}{\partial x_j}\right] + P_\omega - \beta \rho \omega^2 + 2(1 - f_1)\frac{\rho \sigma_{\omega 2}}{\omega}\frac{\partial k}{\partial x_j}\frac{\partial \omega}{\partial x_j} \tag{13}$$

where k and ω are the turbulent kinetic energy and the specific dissipation rate of turbulence, and P_k and P_ω denote the corresponding production term respectively. P_k and P_ω are defined as follows:

$$P_k = \mu_t \Omega^2, P_\omega = C_\omega \rho \Omega^2 \tag{14}$$

where Ω is the magnitude of vorticity and μ_t is the eddy viscosity,

$$\mu_t = \frac{a_1 \rho k}{\max(a_1 \omega, f_2\|\Omega\|)} \tag{15}$$

The constants $\sigma_k, \sigma_\omega, \beta$ and C_ω are calculated via

$$\phi = f_1 \phi_1 + (1 - f_1)\phi_2, f_1 = \tanh\left(\Gamma_1^4\right)$$
$$\Gamma_1 = \min\left[\max\left(\frac{500\mu}{\rho \omega d^2}, \frac{\sqrt{k}}{0.09\omega d}\right), \frac{4\rho \sigma_{\omega 2}k}{CD_{k\omega}d^2}\right] \tag{16}$$
$$CD_{k\omega} = \max\left(2\frac{\rho \sigma_{\omega 2}}{\omega}\frac{\partial k}{\partial x_j}\frac{\partial \omega}{\partial x_j}, 1 \times 10^{-20}\right)$$

where d is the nearest distance to the wall. The constant a_1 is set to be 0.31. f_2 takes the form

$$f_2 = \tanh\left(\Gamma_2^4\right), \Gamma_2 = \max\left(\frac{2\sqrt{k}}{0.09\omega d}, \frac{500\mu}{\rho \omega d^2}\right) \tag{17}$$

The two sets of coefficients ϕ_1 and ϕ_2 chosen from the original $k - \omega$ model and $k - \epsilon$ model respectively, are as follows:

$$\sigma_{k1} = 0.85 , \ \sigma_{\omega 1} = 0.5 , \ \beta_1 = 0.075 , \ C_{\omega 1} = 0.5332$$
$$\sigma_{k2} = 1.0 , \ \sigma_{\omega 2} = 0.856 , \ \beta_2 = 0.0828 , \ C_{\omega 2} = 0.4403 \tag{18}$$

2.3 Discretization

The finite volume method is employed in this paper, the compressible Navier-Stokes equations are discretized on the multi-block structured grids. Based on its robustness and high resolution of stationary discontinues, Edwards' low diffusion flux splitting scheme (LDFSS) [13] is adopted for the inviscid flux vectors. The viscous flux vectors are calculated with second order central difference scheme. The implicit LUSGS method is employed for time marching. In order to meet the computational requirements and

improve computational efficiency, Massage Passing Interface (MPI) is involved for massive parallel computation. Different combinations of Pr_t and Sc_t are introduced with SST turbulence model mentioned above.

3 Code Validation

A test model Hyshot, performed in T4 shock tunnel facility at University of Queensland [14], is chosen to validate the above numerical methods and displayed in Fig. 1. A sequence of wind-tunnel experiments have been performed under various flow conditions and one of the experimental "fuel on" case is selected in this study. In order to reduce the computational cost, a two-dimensional configuration is employed in this paper as which used widely in previous researches. For the dimensional simplification, the injection hole is simplified to be a slot with the approximate length as 2.6 mm and the rest of the main combustor geometry stays the same.
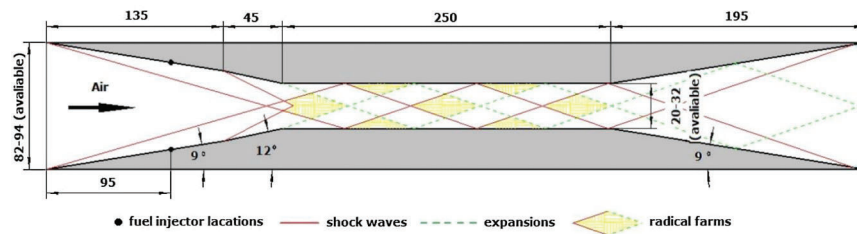
Figure 1: Schematic description of the experimental scale scramjet model Hyshot [14]

3.1 Geometry and Flow Conditions

The referenced flow conditions for code validation are tabulated in Tab. 1. The wall boundary conditions are set as standard no-slip and adiabatic wall. Air including 23.31% oxygen and 76.69% nitrogen is modeled instead of perfect gas model. All the numerical methods described above with a constant Pr_t as 0.7 and a constant Sc_t as 0.9 are performed in this validation case.

Table 1: Freestream flow conditions for the validation case

	Ma_∞	$\alpha_\infty(deg)$	$T_\infty(K)$	$P_\infty(Pa)$	Y_{H_2}	Y_{O_2}	Y_{N_2}
Air	6.42	0.0	412.0	8958.0	0.0	0.2331	0.7669
H_2	1.0	54.0	300.0	64000.0	1.0	0.0	0.0

3.2 Grid Sensitivity Analysis

As shown in previous studies, grid spacing in the wall normal direction is highly critical in numerical simulations for reliable results, especially in the region near solid wall. Drawing lessons from the previous numerical experience, the grid Reynolds number which determines the first cell height by controlling the grid scale [15], is introduced here:

$$Re_\Delta = \frac{\rho_\infty u_\infty \Delta}{\mu_\infty} \tag{19}$$

where $\rho_\infty, u_\infty, \mu_\infty$ are the freestream density, velocity and viscosity respectively, Δ denotes the first grid scale on the solid wall in the wall normal direction.

The grid convergence needs to be verified firstly to ensure the reliability of the following computations. Three different grid spacing scales with respect to empirical grid setting strategy [16], namely coarse,

Table 2: Detailed information of grid system

	Coarse grid	Medium grid	Fine grid
Δ(mm)	0.0075	0.005	0.0025
Re_Δ	60	40	20
Cell Number	48560	60600	72640

Figure 2: Topology of the medium grid for the two-dimensional Hyshot geometry

medium and fine grid, are employed to indicate the grid independence. The detailed grids information is tabulated in Tab. 2. and the distribution of medium grid is displayed in Fig. 2 particularly.

Fig. 3 illustrates the pressure contours distribution of the full configuration, in which the top half is mirrored by the bottom half for better observation. It can be seen that the ramp shocks impinge clearly on each other and two symmetrical strong shocks generate after interaction. Afterwards, the shocks interact with the expansion waves forming at the entrance of the combustor and two separation bubbles can be observed clearly near the throat. The separation shocks reflect between the upper wall and the lower wall and make the boundary layer separate, which brings in a shock-train like structure and some diamond structures form throughout the remaining combustor. Fig. 4 shows the H_2O contours distribution of the full configuration, which represents whether the engine can ignite successfully and whether the combustion efficiency meets the design requirement.
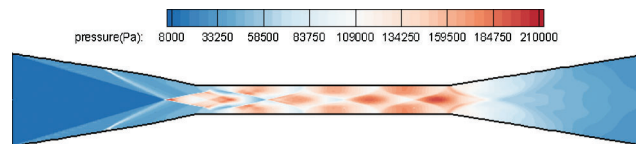
Figure 3: Pressure contours of the full configuration for the two-dimensional HyShot geometry
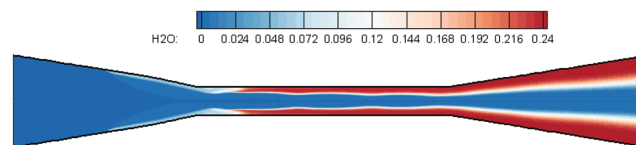
Figure 4: H2O contours of the full configuration for the two-dimensional HyShot geometry

The numerical results are quantitatively compared with the experimental data and the comparison results are illustrated in Fig. 5. The static pressure distribution along one of combustor walls is plotted. The profiles obtained from all the three different grid spacing scales match the experimental data quite well. The pressure profiles jump up and down along the combustor wall because of the shock reflections, which reveals the shock-train like structure illustrated in Fig. 1. The good consistency between the numerical results and experimental date, including the jumping positions, represents that both the position of shock wave and
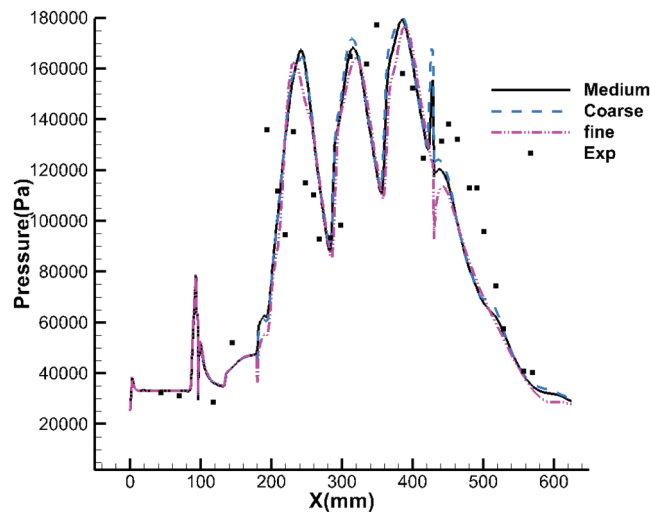
Figure 5: Pressure distribution along the lower wall, compared with experimental data

its reflection have been numerically captured well. The qualitative and quantitative comparisons demonstrate that, the numerical approach and the strategy for grid spacing can provide reliable results for supersonic combustion simulation. Meanwhile, in consideration of numerical precision and computational cost, the medium grid is employed next to evaluate the flow field since there is no significant difference between the medium grid solution and the fine grid solution.

4 Computational Details

In the present work, in particular, two test cases with different characteristics are chosen for further evaluation of the role played by these two parameters: Burrows-Kurkov case [17] and DLR case [18]. The Burrows-Kurkov case focuses on the supersonic turbulent combustion occurring inside the boundary layer. The DLR case is a famous reference case since plenty of experimental and numerical investigations have been performed. Therefore, both of the two cases are appropriate for further study.

4.1 Burrows-Kurkov Case

Burrows-Kurkov case [17] examines a finite-rate with hydrogen-air chemical reactions occurring in Mach 2.44 vitiated air. The turbulence/chemistry interactions play a very important role in the prediction of self-ignition process since it is strongly influenced by the wall cooling effect. The supersonic combustion near the wall is quite sensitive to the development of boundary layer. Thus, the ignition points and temperature values at the combustor outlet are investigated.

4.1.1 Geometry and Flow Conditions

The schematic experiment configuration and computational grid are illustrated in Fig. 6. The minimum grid spacing on all the walls is 5×10^{-3} mm. Additionally, all the walls are set as isothermal with $T_w = 300$ K. The flow conditions are listed in Tab. 3.

4.1.2 Results and Discussions

Nine individual cases are computed under various setting manner for Pr_t and Sc_t in this study. The specific parameters for each case are presented in Tab. 4. It can be seen that the ignition occurring at quite a distance downstream from the injection point, representing a typical ignition-delayed phenomenon. The ignition locations for each case are tabulated in Tab. 4. Meanwhile, the maximal temperature and H_2O mass fraction of the whole combustor obtained via numerical simulation are also
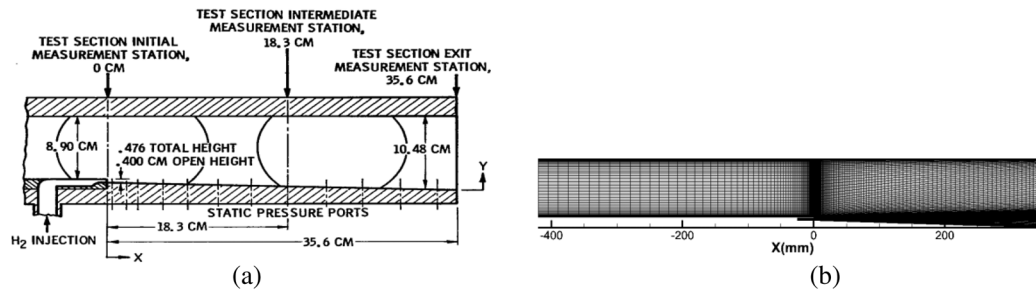
Figure 6: Schematic description of the experimental configuration and topology of the grid for Burrows-Kurkov geometry

Table 3: Freestream flow conditions for the Burrows-Kurkov case

	Ma_∞	$\alpha_\infty(deg)$	$T_\infty(K)$	$P_\infty(Pa)$	Y_{H_2}	Y_{O_2}	Y_{H_2O}	Y_{N_2}
Air	2.44	0.0	1270.0	100000.0	0.0	0.258	0.256	0.486
H_2	1.0	0.0	254.0	100000.0	1.0	0.0	0.0	0.0

Table 4: Statistics data for all the Burrows-Kurkov cases

	Pr_t	Sc_t	$Ignition(mm)$	$T_{max}(K)$	H_2O_{max}
case1	0.5	0.5	125.0	2210.73	0.4982
case2	0.5	0.7	140.0	2118.86	0.4996
case3	0.5	0.9	156.0	2084.03	0.5006
case4	0.7	0.5	100.0	2303.56	0.4941
case5	0.7	0.7	111.0	2193.81	0.4970
case6	0.7	0.9	125.0	2122.82	0.4971
case7	0.9	0.5	90.0	2389.18	0.4920
case8	0.9	0.7	100.0	2286.56	0.4946
case9	0.9	0.9	102.0	2190.48	0.4942

tabulated in Tab. 4. It can be seen that the self-ignition point alters between X = 90 mm and X = 156 mm with the variation of Pr_t and Sc_t. The lower Pr_t and the higher Sc_t bring in further back ignition location. The maximal temperature decreases along with the increase of Sc_t and seems to have no concern with Pr_t. The two parameters seemingly have little effect on the maximal H_2O mass fraction, which implies that turbulent transport process does not significantly affects chemical reaction process within finite rate chemical model framework.

Fig. 7 displays the temperature contours in the combustor. It can be seen obviously that the self-ignition point alters in different cases and there are significant differences of the temperature distributions among these cases. Fig. 8 presents the distributions of flow field variables together with the experimental data at the exit for all cases, including temperature and H_2O mass fraction. It also shows that temperature distribution is more sensitive to these two parameters than H_2O mass fraction.
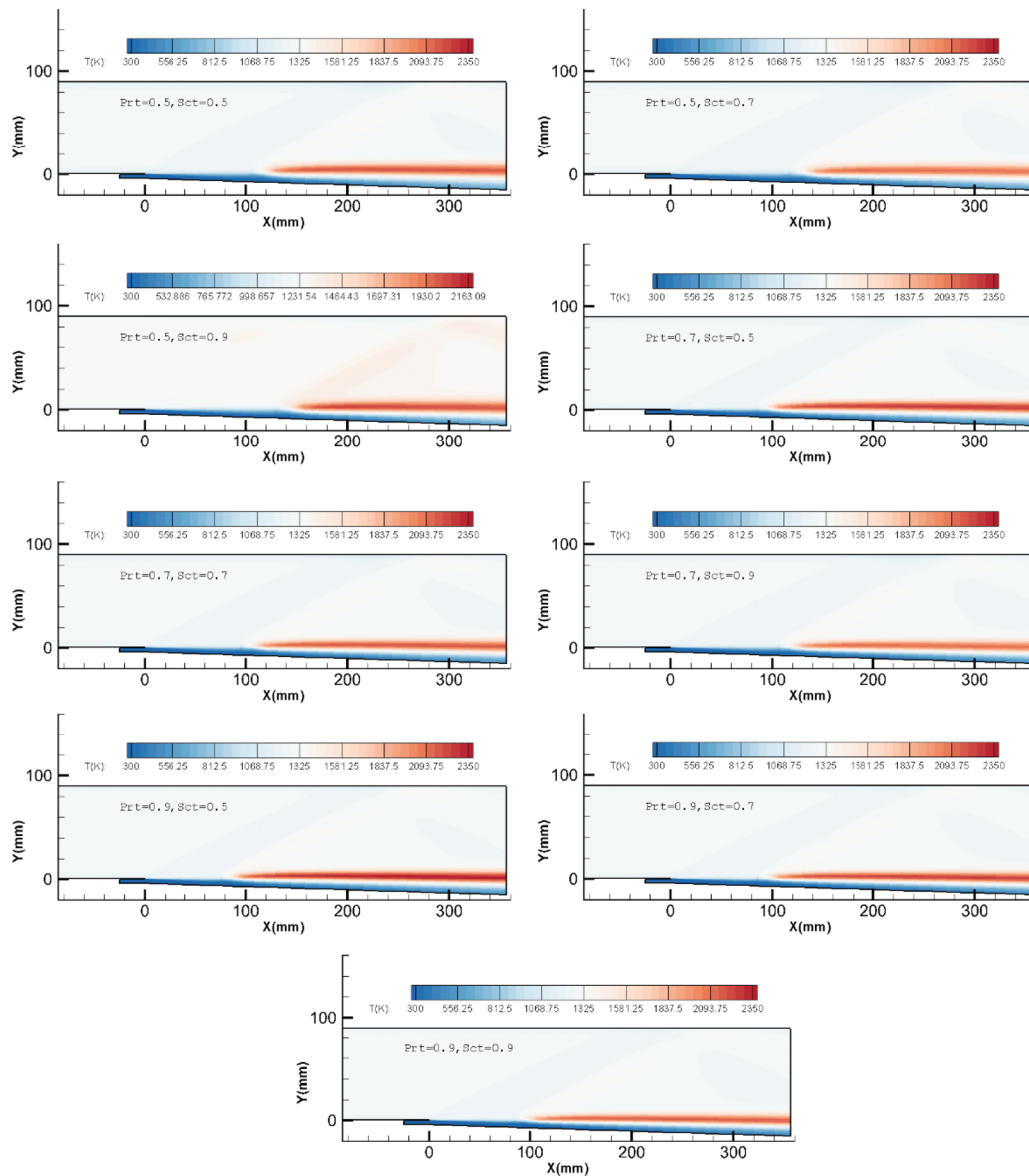
Figure 7: Temperature contours for all the Burrows-Kurkov cases

4.2 DLR Case

As a typical and famous supersonic combustion ramjet with strut-based injection system, the case similar to DLR's experimental configuration has been extensively studied. In particular, the velocity and temperature distribution data are very significant and useful for comparison and validation.

4.2.1 Geometry and Flow Conditions

A three-dimensional configuration of the DLR case is employed in order to retain the main properties of the experimental configuration for the RANS simulation. The full configuration with 15 spanwise holes is simplified instead by a smaller configuration with one half injector hole and half the domain between two-adjacent holes. It is considered sufficient enough for RANS simulation to involve the property of spanwise transport and mixing. The side-view schematic of the scramjet combustor and the computational grid are illustrated in Fig. 9. The minimum grid spacing on all the walls is 5×10^{-3} mm, except at the
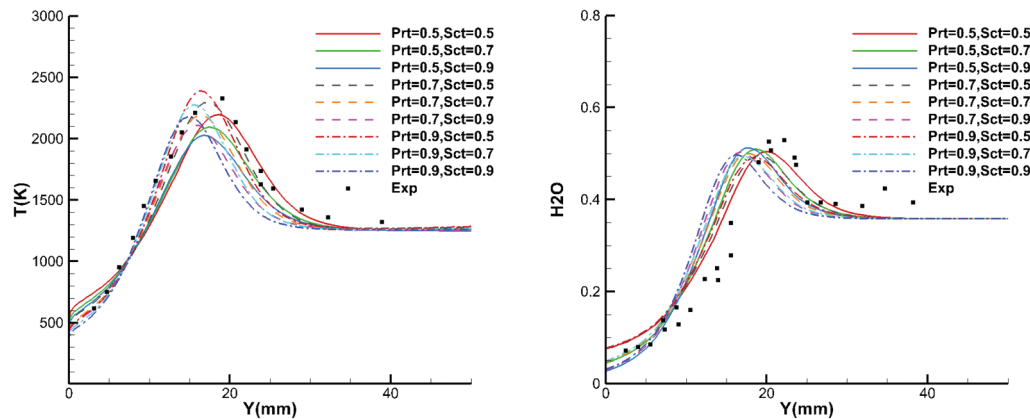
Figure 8: Temperature (left) and H_2O (right) distributions at the exit, compared with experimental data
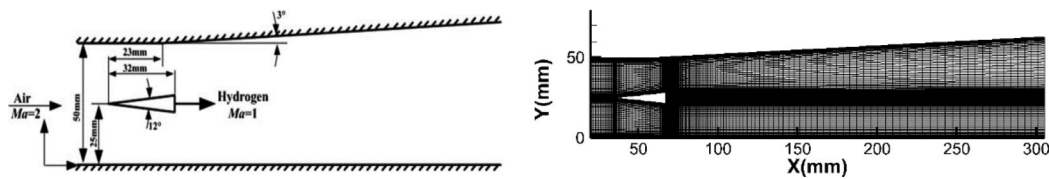
Figure 9: Schematic description of the experimental configuration and topology of the grid for DLR geometry

Table 5: Freestream flow conditions for the DLR case

	Ma_∞	$\alpha_\infty(deg)$	$T_\infty(K)$	$P_\infty(Pa)$	Y_{H_2}	Y_{O_2}	Y_{H_2O}	Y_{N_2}
Air	2.0	0.0	340.0	100000.0	0.0	0.232	0.032	0.736
H_2	1.0	0.0	250.0	100000.0	1.0	0.0	0.0	0.0

injector's back plane, where the minimum spacing is increased to 5×10^{-2} mm. Moreover, all the combustor walls are assumed to be adiabatic in this case. The flow conditions are listed in Tab. 5.

4.2.2 Results and Discussions

Nine individual case simulations are carried out under the same setting manner mentioned above in Burrows-Kurkov cases. The specific setting parameters for each case are tabulated in Tab. 6. It is quite different from the Burrows-Kurkov cases that ignition locations are almost indeclinable in DLR cases, which is probably because of the isothermal wall with $T_w = 300$ K. An obvious self-ignition delay phenomenon exists inside the boundary layer, which is probably because of the strong cooling process by the wall. Meanwhile, the maximal temperature varies irregularly and seems to have no concern with the Pr_t and the Sc_t. However, the maximal H_2O mass fraction varies within such a small range, which also implies that turbulent transport has merely no significant effect on chemical reaction process.

Fig. 10 presents the temperature contours and it is evident that the self-ignition point stays at the position about X = 75 mm. There are some visible differences of the temperature distributions between the cases. Figs. 11 and 12 illustrate temperature distributions and velocity distributions at the cross-section X = 78 mm and X = 125 mm, respectively, together with the experimental data for all cases. As can be seen that the temperature distributions are more sensitive to Pr_t and Sc_t than the velocity distributions.

Table 6: Statistics data for all the DLR cases

	Pr_t	Sc_t	$Ignition$(mm)	$T_{max}(K)$	H_2O_{max}
case1	0.5	0.5	75.0	2323.84	0.2738
case2	0.5	0.7	75.0	2361.53	0.2753
case3	0.5	0.9	75.0	2089.79	0.2766
case4	0.7	0.5	75.0	2475.70	0.2726
case5	0.7	0.7	75.0	2355.21	0.2748
case6	0.7	0.9	75.0	2256.60	0.2759
case7	0.9	0.5	75.0	2562.54	0.2715
case8	0.9	0.7	75.0	2453.00	0.2739
case9	0.9	0.9	75.0	2361.53	0.2753
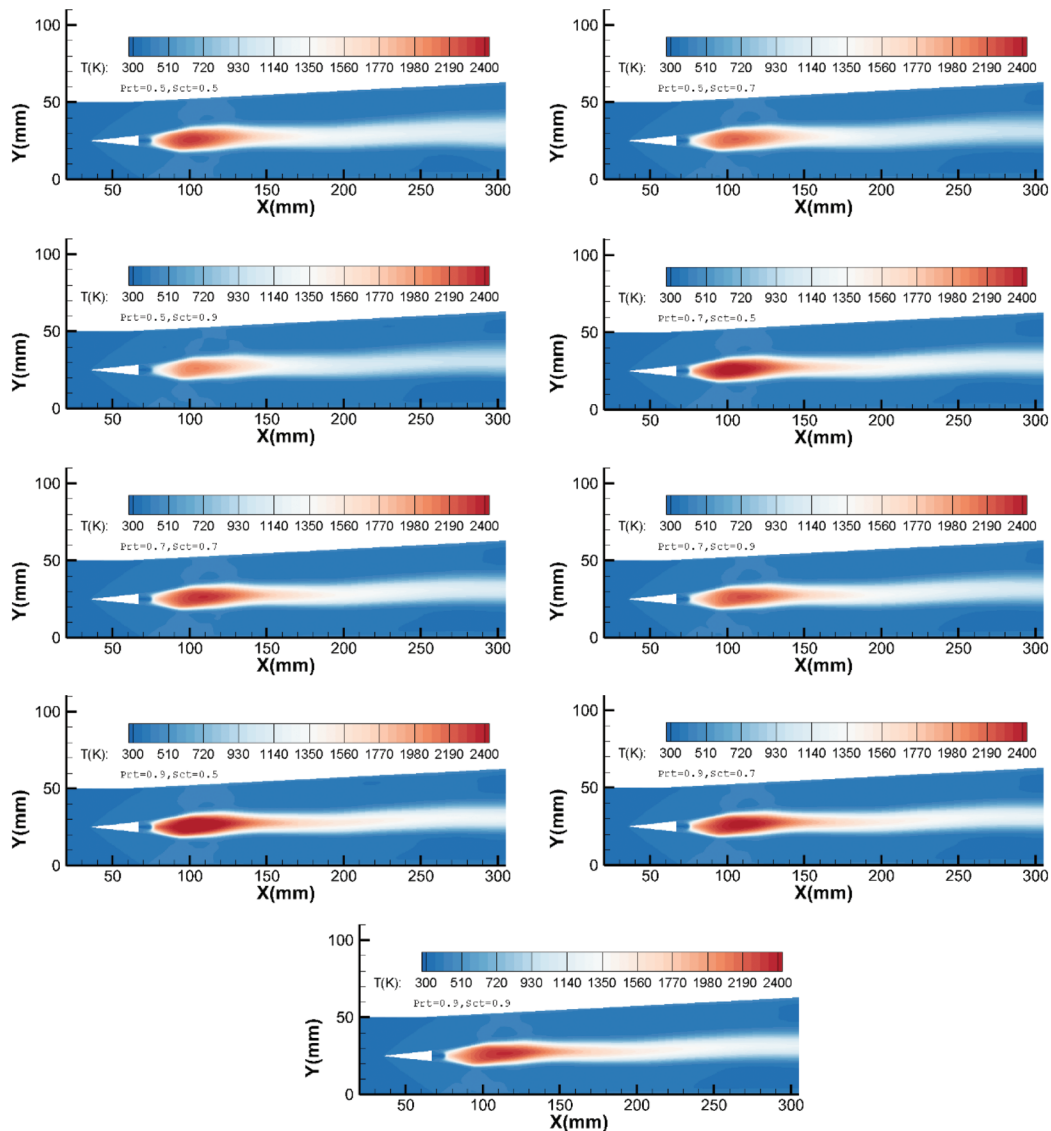
Figure 10: Temperature contours for all the DLR cases
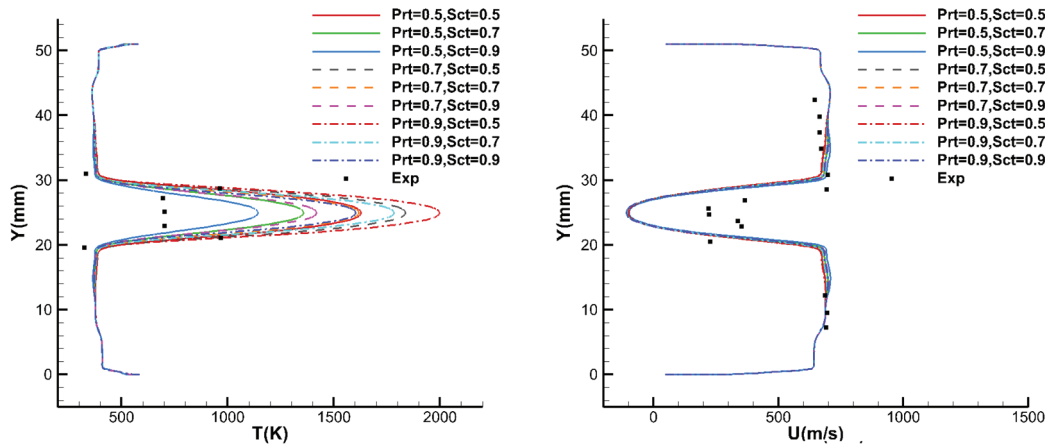
Figure 11: Temperature (left) and X-Velocity (right) distributions at the cross section X = 78 mm, compared with experimental data
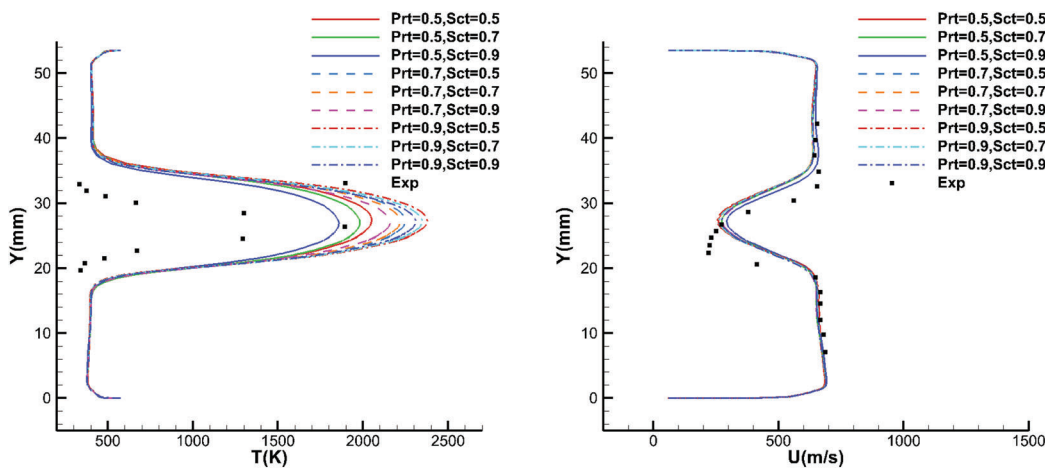
Figure 12: Temperature (left) and X-Velocity (right) distributions at the cross section X = 125 mm, compared with experimental data

5 Conclusion

In the current study, the numerical analysis on the influence of the turbulent Prandtl number Pr_t and the Schmidt number Sc_t on the flow field prediction for scramjet configuration are conducted. Navier-Stokes equations are numerically solved with standard SST turbulence model for turbulent transport process and finite rate model for chemical reaction process. Main conclusions are summarized as follow:

1. In Burrows-Kurkov case, the lower Pr_t and the higher Sc_t bring the ignition location further back. The isothermal wall with cooling process exists inside the boundary layer can strongly delay the self-ignition process. H_2O mass fraction distribution is less sensitive to the Pr_t and the Sc_t, which implies that turbulent transport process have merely no significant effect on chemical reaction process within the finite rate chemical model framework.

2. In DLR case, ignition locations are almost indeclinable because the combustion process occurs almost in the central region of combustor. The maximal temperature varies irregularly and the maximal H_2O mass fraction varies within a small range. The Pr_t and Sc_t affect the distribution of the combustion region,

which in turn changes the temperature distribution. In addition, the intensity of the combustion remained almost constant on account of the almost unchanged maximal H_2O mass fraction.

3. Temperature distribution is more sensitive than H_2O mass fraction and velocity distributions. Since the Pr_t and Sc_t have no significantly effect on chemical reaction process, it implies that the heat conduction and diffusion mechanism have been greatly influenced by these two parameters via turbulent transport and mixing processes. Detailed and in-depth research for this opinion should be investigated for a further step.

Conflicts of Interest: The authors declare that they have no conflicts of interest to report regarding the present study.

References

1. Xiao, X., Hassan, H. A., Edwards, J. R. (2007). Role of turbulent prandtl numbers on heat flux at hypersonic mach numbers. *AIAA Journal, 45(4),* 1415–1423.

2. Eklund, D. R., Baurle, R. A., Gruber, M. R. (2001). Numerical study of a scramjet combustor fueled by an aerodynamic ramp injector in dualmode combustion. *Computers, AIAA Paper.*

3. Baurle, R. A. (2017). Hybrid reynolds-averaged/large-eddy simulation of a cavity flameholder: modeling sensitivities. *AIAA Journal, 55(2),* 524–543. DOI 10.2514/1.J055257.

4. Roy, C. J., Edwards, J. R. (2000). Numerical simulation of a three-dimensional flame/shock wave interaction. *AIAA Journal, 38(5),* 103–124. DOI 10.2514/2.1035.

5. Gao, Z. X., Jiang, C. W., Lee, C. H. (2016). On the laminar finite rate model and flamelet model for supersonic turbulent combustion flows. *International Journal of Hydrogen Energy, 41(30),* 13238–13253. DOI 10.1016/j.ijhydene.2016.06.013.

6. Xiao, X., Hassan, H. A., Baurle, R. A. (2007). Modeling scramjet flows with variable turbulent prandtl and schmidt numbers. *AIAA Journal, 45(6),* 806–813.

7. Ingenito, A., Bruno, C. (2008). LES of supersonic combustion with a variable turbulent schmidt number. *AIAA International Space Planes and Hypersonic Systems and Technologies Conference, 28 April–1 May, Dayton, Ohio.*

8. Jiang, L. Y., Campbell, I. (2009). Prandtl/schmidt number effect on temperature distribution in a generic combustor. *International Journal of Thermal Sciences, 48(2),* 322–330. DOI 10.1016/j.ijthermalsci.2008.03.014.

9. Wilke, C. R. (1950). A viscosity equation for gas mixtures. *Chemical Physics, 18(4),* 517–591.

10. Imlay, S. T., Roberts, D. W., Soetrisno, M. (1992). Nonequilibrium thermo-chemical calculations using a diagonal implicit scheme. *AIAA 29th Aerospace Sciences Meeting, Nevada, USA.*

11. Dandani, M., Lepiller, V., Ghezal, A., Desevaux, P. (2018). Numerical visualizations of mixing enhancement in a 2D supersonic ejector. *Fluid Dynamics & Materials Processing, 14(1),* 23–37.

12. Menter, F. R. (1994). Two-equation eddy-viscosity turbulence models for engineering applications. *AIAA Journal, 32(8),* 1598–1605. DOI 10.2514/3.12149.

13. Edwards, J. R. (1997). A low diffusion flux-splitting scheme for navier-stokes calculations. *Computers and Fluids, 26(6),* 635–659. DOI 10.1016/S0045-7930(97)00014-5.

14. Odam, J. (2014). *Scramjet experiments using radical farming (Ph.D. Thesis).* University of Queensland, Australia.

15. Wang, X. Y., Yan, C., Zheng, W. L., Zhong, K., Geng, Y. F. (2016). Laminar and turbulent heating predictions for mars entry vehicles. *Acta Astronautica, 128,* 217–228. DOI 10.1016/j.actaastro.2016.07.030.

16. Bentarzi, F., Mataoui, A. (2018). Turbulent flow produced by twin slot jets impinging a wall. *Fluid Dynamics & Materials Processing, 14(2),* 107–120.

17. Burrows, M. C., Kurkov, A. P. (1973). Analytical and experimental study of supersonic combustion of hydrogen in a vitiated airstream. *NASA,* 1–24.

18. Guerra, R., Waidmann, W., Laible, C. (1991). An experimental investigation of the combustion of a hydrogen jet injected parallel in a supersonic air stream. *AIAA Third International Aerospace Planes Conference, Orlando, FL, USA, 42(2),* 103–124.